

Upper Mantle Tomographic V_p and V_s Images of the Rocky Mountains in Wyoming, Colorado and New Mexico: Evidence for a Thick Heterogeneous Chemical Lithosphere

Huaiyu Yuan and Ken Dueker

Department of Geology and Geophysics, University of Wyoming, Laramie, Wyoming

Upper mantle tomographic P- and S-wave images from the CD-ROM teleseismic deployment reveal two major lithospheric anomalies across two primary structural boundaries in the southern Rocky Mountains: a ~200 km deep high velocity north-dipping "Cheyenne slab" beneath the Archean-Proterozoic Cheyenne belt, and a 100 km deep low velocity "Jemez body" beneath the Proterozoic-Proterozoic Jemez suture. The Cheyenne slab is most likely a slab fragment accreted against the Archean Wyoming mantle keel during the Proterozoic arc collision processes. If this interpretation is correct, then the ancient slab's thermal signature has been diffused away and non-thermal explanations for the slab's isotropic high velocity signature are required. Tomographic modeling of possible chemical and anisotropic velocity variations associated with the slab shows that our isotropic velocity images can be explained via non-thermal models. In addition, the de-correlation of the P- and S-velocity images and the CD-ROM shear wave splitting modeling [Fox and Sheehan, this volume] are consistent with a dipping slab. The Jemez body plausibly results from the combination of low-solidus materials in the suture lithosphere and the late Cenozoic regional thermal heating of the lithosphere. The 100 km deep lithospheric layering [Zurek and Dueker, this volume] and the uniform shear wave splitting measurements support our contention that the Jemez body is a lithospheric anomaly. A third, less anomalous low velocity structure extends beneath the middle Rio Grande Rift to 300 km depth. This anomaly may manifest a thermal upwelling that could be causing increased heat flow into the lithosphere. Our results suggest that lithospheric heterogeneities related to fossil accretionary processes have been preserved in the Precambrian sutures, and are preferentially affecting the subsequent tectonism of the southern Rocky Mountains.

1. INTRODUCTION

From a global perspective, natural and controlled source seismic imaging of Precambrian suture zones has shown that the sub-crustal lithosphere beneath sutures is often seismically, chemically and anisotropically heterogeneous [Shragge *et al.*, 2002; Judenherc *et al.*, 2002; Shomali *et al.*, 2002; Babuska and Cara, 1991; Balling, 2000; Snyder, 2002; Poupinet *et al.*, 2003; Sandoval *et al.*, 2003a]. Tomographic velocity images reveal sharp lateral variations that often demarcate distinct lithospheric blocks separated by suture zones. Given the old age of suture zones and no obvious variations in modern day heat flow, compositional and anisotropic velocity heterogeneities are required to explain these velocity anomalies. Sub-Moho dipping reflectors observed from the controlled-source imaging studies under suture zones are often explained as fossil slabs [Warner *et al.*, 1996; Eaton and Cassidy, 1996; Pharaoh, 1999; Abramovitz and Thybo, 2000; Gorman *et al.*, 2002; White *et al.*, 2002]. For instance, two uppermost mantle dipping reflectors beneath the Great Fall/Vulcan suture at the northern end of the Wyoming craton have been imaged [Gorman *et al.*, 2002]. Interpretation of the seismic signature and tectonic history of this region suggests that the reflectors are best explained as fossil slabs related to suturing between the Wyoming Province, the Medicine Hat Block, and the Hearne Province. Fossil slabs, whose associated oceanic crust resides in eclogitic facies, are consis-

tent with the observed impedance contrast where detailed petrophysical and seismic modeling has been done [Morgan *et al.*, 2000].

South of the Wyoming craton, good basement exposures exist along a 1000 km wide sequence of Proterozoic oceanic terranes [Karlstrom and Houston, 1984]. Detailed structural, basement age, geochemical, and pressure-temperature time histories allow this region to be divided into a sequence of distinct blocks separated by sutures [Karlstrom and Bowring, 1988; Condie, 1992]. Key to constraining how these blocks accreted and transformed into stable continental lithosphere is accurate imaging of the sub-crustal structures. A large teleseismic experiment was deployed across two primary suture zones in this region: the Archean-Proterozoic Cheyenne belt (imaged by the North line), and the Proterozoic Jemez suture (imaged by the South line). The main target is constraining the seismic lithospheric heterogeneities related to the Proterozoic suturing processes in the southern Rocky Mountains.

Our results show a high velocity north dipping slab-like anomaly (referred to as “the Cheyenne slab” herein) beneath the Cheyenne belt, and a low velocity body (referred to as “the Jemez body”) extending to 100 km beneath the Jemez suture. We interpret the Cheyenne slab as a fossil Proterozoic slab fragment accreted against the Archean Wyoming margin. The Jemez body is most likely preferentially molten low-solidus materials trapped in the suture lithosphere. At the same time, upper mantle convective rolls [Richter, 1973] may be focusing heat along the NE-trending Jemez suture [Dueker *et al.*, 2001].

2. TECTONIC SETTING

The relevant geologic history of the southern Rocky Mountains in the western United States begins with rifting of the southern margin of the Archean Wyoming province at 2.1 Ga [Karlstrom and Houston, 1984], followed by 300 Ma of passive margin sediment accumulation. Proterozoic arc accretion began when the Green Mountain arc accreted to the Wyoming craton at 1.78 Ga [Chamberlain, 1998] to create the Archean-Proterozoic suture known as the Cheyenne belt. Accretion of Proterozoic island arcs continued to the south until 1.65 Ga when the Mazatzal terrane accreted to the southern margin of the Yavapai terrane to form the Jemez suture [Karlstrom and Bowring, 1988; Wooden and DeWitt, 1991; CD-ROM Working Group, 2002]. Post 1.65 Ga, the primary magmatic event preserved in the basement rocks is the pervasive exposure of 1.4 Ga granitic batholiths whose petrogenesis most plausibly requires the emplacement of a large volume of mantle derived magma into the lithosphere [Williams *et al.*, 1999]. In addition, Laramide aged calc-alkaline magmatism modestly affected this region along with a significant peak in volcanism in Colorado and New Mexico around 35 Ma [Armstrong and Ward, 1991]. Two compressional events, the Pennsylvanian Ancestral Rockies [Kluth and Coney, 1981] and the late Cretaceous Laramide [Hamilton and Myers, 1966] orogenies, significantly deformed the Proterozoic and Archean aged lithosphere. While debated, it appears that the later shortening event did reactivate the Precambrian structures, and produced basement uplifts and deep sediment basins in the southern Rockies. Rifting of the lithosphere along the N-S trending Rio Grande rift [Chapin, 1979] started in the late Oligocene to early Miocene time. Associated rift-related magmatic activity is relatively minor, except along the late-Tertiary Jemez volcanic lineament. This volcanic lineament appears to be roughly following the trend of the Proterozoic Jemez suture [CD-ROM Working Group, 2002; Wooden and DeWitt, 1991; Shaw and Karlstrom, 1999].

The modern day geophysical characteristics of the Proterozoic Rocky Mountains (i.e., south of the Wyoming/Colorado border) are distinct with respect to the Archean Wyoming province as evidenced by its higher elevations, higher heat flow [Decker *et al.*, 1988], on-going rifting [Ingersoll *et al.*, 1990], and volcanism [Aldrich and Laughlin, 1984; Baldrige *et al.*, 1995]. In the upper mantle, the seismic shear wave velocity increases from very slow in southern New Mexico to slightly slower than the global average beneath the Wyoming province [Deep Probe working group, 1998; Goes and van der Lee, 2002]. Thermal calculations from the surface wave tomographic images suggest that the upper mantle beneath this region is at or near the dry peridotite solidus [Goes and van der Lee, 2002]. An interesting observation in the intermountain western U.S. is the spatial correlation between the young volcanic fields and Proterozoic suture zones [Dueker *et al.*, 2001; Karlstrom and Humphreys, 1998; CD-ROM Working Group, 2002]. These suture zones are generally underlain by low velocity upper mantle anomalies. Whether the low velocity anomalies represent compositional variations in the lithosphere or thermal effects of upwelling asthenosphere or some combination of both is still poorly constrained [Dueker *et al.*, 2001].

3. TELESEISMIC TRAVEL-TIME PROCESSING

3.1 Travel-time Residual Measurement

The CD-ROM teleseismic experiment consists of a deployment of two dense (average 12 km station spacing) broadband arrays of 25 sensors each across the Cheyenne belt and the Jemez suture (Figure 1). The one-year deployment from May 1999 to June 2000 creates a dataset with good earthquake azimuthal and ray parameter coverage. Arrivals of P, S, PP, SS, PcP, ScS, PKiKP and SKS_{ac} phases from Aleutian, west Pacific, Tonga and south America are measured to obtain a diversity of ray sampling for the tomographic inversion. Both P- and S-waveforms are band-pass filtered (0.05 Hz – 0.3 Hz) to minimize the background noise, and to avoid the frequency dependent attenuation effects that may affect the scaling between P- and S-velocities [Warren and Shearer, 2000]. The radially symmetric IASPEI-91 velocity model [Kennett and Engdahl, 1991] is used to calculate the predicted moveout associated with the arrivals for each event. A time window of 4- and 6-s for the P- and S-waveform cross-correlation window is found to give robust residual estimates.

The travel-time residuals are measured using the multi-channel cross-correlation technique, which gives robust residual measurements and standard errors [VanDecar and Crosson, 1990; Allen *et al.*, 2002]. For each event, cross-correlation functions for all waveform pairs are computed, and the time lag associated with the peak value of each cross-correlation function is calculated. Given n waveforms, this process results in a data vector of $\frac{1}{2}n(n-1)$ time shifts between station pairs. By adding a constraint equation that the mean residual associated for an event is zero, this system of equations becomes over-determined and is solved via a least-squares algorithm. For the P- and S-waves, the number of measured relative residuals is 4032 and 2058 with average standard error of 0.05 and 0.1 s, respectively. Noteworthy is that by forcing the mean of each event's residuals to zero, it creates a relative travel-time residual dataset that can only recover relative velocity variations, not absolute velocities.

Simple statistical analysis is performed to identify bad residuals with large error and spurious time shift. The primary cause of the bad residuals is due to measurement of low signal to noise ratio seismograms. These data are easily identified and removed by their large standard error from the cross-correlation solution. Study of the relation between the wave shape coherency and the standard error suggests that 0.15 and 0.3 s are reasonable thresholds for rejecting data for the P- and S-residuals, respectively. The secondary cause of the bad data is due to shifted waveforms by faulty station clocks that resulted in a few spurious travel-time measurements. These types of outliers are easily identified via spatial residual analysis (residual vs. station latitude plot). For each event, the misfits between the event data and a robust least-square quadratic polynomial fit are calculated. Then spurious travel-times are found and removed when their value is greater than twice the standard variation ($> 2\sigma$) of the polynomial fit. The last step to identify bad data is via slowness residual analysis (polar plot). The residuals for each station are binned into non-overlapping grids in 2-D slowness space and the differences between the bin median and individual residuals are calculated. Then, individual residuals with large time differences ($> 2\sigma$) are removed.

3.2 Choice of an S-wave Particle Motion Coordinate System

Unlike for the P-waves, where the residuals are measured on the vertical channel of the seismometer, it has to be decided which particle motion system to use in measuring the travel-time residuals for the S-waves. Typical choices include the SH component, the average fast or slow anisotropy axis detected from shear wave splitting, or the maximum particle motion direction. The SH component waveform is least contaminated by the scattering from near station structures, and is generally the “cleanest” coordinate system. However, exclusive use of SH results in a significant reduction in available data. In passing through an anisotropic volume, the SV and SH components of ground motion become coupled, causing their waveforms to become distorted which can bias the residuals measured via waveform cross-correlation. If a uniform anisotropic layer is present beneath the seismic stations, the waveform distortion and time shift are uniform for each event. The time shifts imparted to the residuals therefore can be removed via demeaning of the residuals. The average fast or slow anisotropic velocity axis is commonly used [e.g., Toomey *et al.*, 1998] when a uniform anisotropic layer exists. If the anisotropic domain varies along the array, demeaning of the residuals cannot remove the travel-time effect of the seismic anisotropy due to the non-uniform distortion of the waveforms, and the biased residuals can create imaging artifacts. In the maximum particle motion coordinate system, the horizontal waveforms are projected onto the first principal component [e.g., Jackson, 1991] of ground motion. This produces a shear waveform dataset that possesses the maximum signal amplitude and hence the greatest number of measurable shear waves travel-times.

Given that the shear wave splitting results shows that the seismic anisotropy domain is uniform beneath the south line and changes to back-azimuthal dependent across the Cheyenne belt [Fox and Sheehan, this volume], the S-wave travel-time residuals are measured in both the maximum particle motion direction, and the average fast velocity axis orientation (N50°E approximately parallel to the North America plate motion direction). Inversion results of both datasets are compared and discussed in section 4.6.

4. TOMOGRAPHIC INVERSION

4.1 Summary ray Dataset

Obtaining comparable V_p and V_s images is important to address the thermal and/or non-thermal causes of the observed upper mantle velocity anomalies [Sobolev *et al.*, 1999; Goes and van der Lee, 2002; Schutt and Humphreys, in press]. Making a summary ray dataset from the raw dataset allows very similar ray sets and hence very similar resolution matrices for both the P- and S-wave inversions [e.g., Schutt and Humphreys, in press]. To make our summary ray datasets for each station, all residuals from all back-azimuth are binned in 2-D horizontal slowness space. The summary ray bin size is an adjustable parameter. It is found in this study that 0.01 s/km and 0.015 s/km for the P- and S-waves summary ray bin size provides a reasonable trade-off between smoothing of the dataset and still having enough residuals within each bin to get a robust mean residual and standard error estimate. A summary ray residual is the weighted mean of the raw residuals at each summary ray point. The weighting function is a Gaussian function with a half width equal to the bin size. This procedure produced nearly identical datasets of ~1200 P- and S-wave summary rays from the original P- and S-wave residuals.

4.2 P- and S-wave Residual Patterns

The P- and S-wave summary ray residuals show large spatial and back-azimuth dependent variations along the CD-ROM transect (Figure 2). The north line has early residuals (0.27 s and 0.63 s average for the P- and S-waves, respectively), and the south line has late residuals (-0.20 s and -0.85 s average, respectively). The peak-to-peak magnitude in the P- and S-residuals is 1.4 s and 3.7 s, accordingly. These large variations in residual patterns require large velocity anomalies in the upper mantle. A simple model to match the magnitude of these residuals would require a 5% (V_p) and 10% (V_s) velocity variation over a 200 km thick layer. If these residuals were purely crustal, implausibly large velocity variations (i.e., ~15% and 30% for P- and S-waves, respectively) would be required. The large azimuthal variation in residuals across the Cheyenne belt and the Jemez suture (CB and JT, respectively in Figure 2a and b) fundamentally require sub-crustal velocity anomalies. Crustal velocity variations cannot produce such large azimuthal variations due to the shallow depth.

4.3 Inversion Method

A linearized inversion for a 2-D velocity model is used to invert the travel-time residuals for structure. The dimension of our model space is 1600 km long by 300 km in depth. Each model block is 10 km (horizontal) by 15 km (depth). The Tectonic North American (TNA) shear wave model [Grand and Helmberger, 1984] is used as the S-wave background velocity model, and the P-wave model is computed assuming a 1.84 V_p/V_s ratio. Rays are traced from each event-receiver pair using the slowness computed from the IASPEI-91 velocity model [Kennett and Engdahl, 1991].

To find an optimal model m , the following matrix equation is solved via full matrix inversion

$$C_d^{-1/2} A S^{-1} S m = C_d^{-1/2} d, \quad (1)$$

where A is the data kernel containing the ray path length in each model block, m the slowness perturbations, d the travel-time residuals, C_d the diagonal a priori data covariance matrix, and S a 3 by 3 nearest neighbor smoothing matrix [Meyerholtz *et al.*, 1989]. The full model resolution and covariance matrices are calculated from the inverse matrix. A range of damping parameters is used to study the trade-off between resolution and model variance reduction. Empirically, the optimal model is at the “elbow” of the model energy versus the resolution spread curve, which is controlled by the damping parameter. The preferred inversion results (Plate 2a and b) are slightly over-damped to minimize artifacts in the images.

4.4 Resolution of Crustal Versus Mantle Velocity Anomalies

An important concern in teleseismic tomography is the separation of the crust and mantle velocity anomalies. The degree of concern is conditioned by the resolving power of the seismic ray set and the relative contribution of the travel-time anomalies from the crust versus the mantle. Given the large station spacing in most teleseismic tomogra-

phy studies, two approaches have been proposed to address the crustal effects: either by adding station static term to absorb shallow structures [Dziewonski and Anderson, 1983], or by removing the crustal travel-times using an a priori crustal model [e.g., Sandoval et al., 2003b]. With large station spacing (i.e. > 20 km), the station static term absorbs not only the crustal travel-time variations, but also mantle structures, and therefore is not used in some studies [Dueker et al., 1993; Sandoval et al., 2003b].

The CD-ROM stations are densely spaced (average 12 km spacing), indicating that crustal scale velocity anomalies can be well resolved. To examine the resolving power of our ray set, a suite of tests on models with various combinations of crust and upper mantle velocity heterogeneity patterns is performed. Two end-member models are presented that are parameterized by the amplitude ratio (θ) of the crust to mantle anomalies, and spatial wavelength (λ_c and λ_m for crust and mantle, respectively) of sinusoidal velocity anomaly variations. The crustal model has $\theta = 3$, $\lambda_c = 30$ km and $\lambda_m = 90$ km (Plate 1a). The mantle model has $\theta = 1/2$, $\lambda_c = 60$ km and $\lambda_m = 90$ km (Plate 1c). Gaussian distributed noise is added that is scaled to 10% RMS (root-mean-square) amplitude of the synthetic residuals. This 10% value is estimated from the noise to signal ratio of the CD-ROM dataset. All synthetic models are inverted with the same damping parameter as in the inversions presented in Plate 2. The inverted crustal model image (Plate 1b) reconstructs an average 70% of the input crustal velocity structure. The inverted mantle model image (Plate 1d) reconstructs 60-70% of the input mantle structure. The amplitudes of the recovered crustal anomalies vary with respect to the amplitude variation of the mantle anomalies. For instance, the reconstructed crust amplitude is higher than the input where the crustal and mantle anomalies are in-phase (the signs for the crustal and mantle anomalies are the same), and the amplitude vanishes where the crustal and mantle anomalies are out of phase. The constructive and destructive effects indicate that vertical smearing of the long wavelength mantle anomalies into the crust is significant.

These synthetic tests demonstrate that when the crustal anomalies dominate, the crustal structure is well reconstructed. On the other hand, if large mantle anomalies exist, false crustal anomalies can be generated. Given that the integrated travel-times from the crustal velocity heterogeneity [Magnani and Levander, this volume; Snelson et al., this volume] is much smaller (~10% of the residual RMS amplitude) with respect to the mantle, the mantle structures are readily smeared into the crust in our inversions. Therefore, we choose to weight the crust and mantle model parameters differently to minimize the mantle smearing in our inversions. This is done by re-weighting the crustal part of the smoothing matrix S in equation (1) to 10% of the mantle parameter value. Comparison of the inversions with and without the crust down-weighted shows insignificant difference in the mantle. The difference in data variance reduction is only 2%, supporting our contention that the contribution of crustal velocity anomalies to our dataset is minor.

4.5 P- and S-wave Inversion Results

The two primary anomalies in the V_p and V_s images (Plate 2a and b) are the high velocity Cheyenne slab beneath the Cheyenne belt, and the low velocity Jemez body beneath the Jemez suture. The Cheyenne slab anomaly extends from the Moho to ~200 km at a 45° dip. In the V_s image, the slab anomaly is not as continuous as in the V_p image. In section 4.6, we show that this de-correlation of the P- and S-images may result from the effect of dipping anisotropy. The Jemez low velocity anomaly is 100 km wide and extends to 100 km depth. A third velocity anomaly is the low velocity “pipe” beneath the south line, which is more continuous in the V_s image. This pipe extends to the bottom of our model space, with its surface projection beneath the San Luis basin of the middle Rio Grande rift.

The standard model error and the resolution matrix (Plate 2c and d) indicate that the velocity anomalies discussed above reside in a region of low standard model error and high resolution. Because the V_p and V_s images are constructed with the summary ray sets, the resolution kernels are very similar for both images. Selected P-image resolution kernels (Plate 2c) demonstrate that the lateral and vertical resolution is good with kernel amplitudes decaying to 40% in 30 km horizontal and 50 km vertical distances. The average standard errors associated with the Cheyenne slab and the Jemez body are ~0.6% and ~0.8% in the V_p and V_s images. The low velocity pipe anomaly extends to the base of the model where the error is larger (0.9% in the V_s), yet still much smaller than the pipe’s 2% S-wave anomaly. The south-dipping direction is opposite to the smearing predicted by the resolution kernel, indicating that the pipe is not a resolution artifact.

4.6 Comparison of S-wave Images From Different Datasets

At sub-solidus absolute temperatures, a thermal anomaly is generally expected to affect the V_p and V_s variations in a linearly scaled manner [Karato, 1993]. Hence, the de-correlation between the V_p and V_s images of the Cheyenne

slab (Plate 2a and b) may indicate non-thermal mantle velocity variation. Melts, fluids and seismic anisotropy variations in mantle can decorrelate the V_p and V_s variations [Karato and Jung, 1998; Sobolev *et al.*, 1999; Goes and van der Lee, 2002]. Given that the CD-ROM shear wave splitting modeling is consistent with a north dipping fast axis anisotropy across the Cheyenne belt [Fox and Sheehan, this volume], the de-correlation of the Cheyenne slab V_p and V_s anomaly may largely result from dipping seismic anisotropy.

One way to assess this dipping anisotropy's effects on our tomographic images is to invert the two S-wave residual datasets, measured in the average fast axis direction and the maximum polarization direction coordinate system. Due to the use of summary ray technique, the two inversions have similar variance reductions of 79% and 81%, respectively, and similar model standard errors and resolution kernels. However, the two S-wave velocity images are significantly different with respect to each other and the P-wave image of the Cheyenne slab (Figure 3). In the two different S-wave images, the slab is imaged as a continuous feature in the average fast axis coordinate system, while it breaks into segments in the maximum particle motion direction system. For an isotropic velocity anomaly, the two S-wave images are expected to be identical. The de-correlation of the two S-images would be consistent with non-isotropic velocity variation such as a dipping anisotropic slab across the Cheyenne belt.

4.7 Synthetic Forward Modeling of Dipping Anisotropy

When anisotropic velocity variations are present, large velocity artifacts are possible in isotropic tomographic inversion. A dipping anisotropic velocity structure results in inconsistent residuals as rays sample the fast and slow velocity axis. As a result, fast and slow velocity artifacts that are perpendicular to each other are present in the inverted P-wave image [Sobolev *et al.*, 1999].

To assess the effects of a dipping anisotropic velocity structure upon our P-wave isotropic inversion, residuals from a set of synthetic slab models are calculated and inverted. The synthetic slab coincides with the 2% contoured region of the inverted P-wave Cheyenne slab (thick contour lines in Plate 3a – d). The three input models are: an isotropic slab, an anisotropic slab, and a third model which is the combination of the first two models. The isotropic slab has a 2% high velocity anomaly. The anisotropic slab has an 8% peak-to-peak velocity variation, with its fast velocity axis fixed at the values from the shear wave splitting modeling [Fox and Sheehan, this volume]: the fast axis strikes $N45^\circ W$ and dips at 45° . The 8% anisotropy specified for the slab is in the range of the computed and measured peridotite aggregates in the mantle [Soedjatmiko and Christensen, 2000; Saruwatari *et al.*, 2001; Babuska and Cara, 1991]. Gaussian noise scaled to 10% RMS amplitude of the synthetic travel-times is added. For simplicity, only the Cheyenne slab is modeled in our synthetic tests.

The inversion well reconstructs the synthetic isotropic slab (Plate 3a). Vertical smearing occurs slightly at the bottom of the slab. As expected, the isotropic inversion cannot recreate the input anisotropic slab (Plate 3b). The inverted image shows two high velocity bodies in-line with the fast symmetry axis (the labeled F axis of the ellipsoid velocity tensor in Plate 3b), and two slow velocity bodies (labeled as 1 and 2) along the slow symmetry axis (the S axis in Plate 3b). A third slow velocity anomaly is present along the slow axis near the bottom of the model space). These three low velocity bodies are consistent with the ones in the observed P-wave image (Plate 3d). The inverted image for the third model (Plate 3c) gives the best match to the observed images: the Cheyenne slab and the associated low velocity bodies (1, 2 and 3 in Plate 3d). Given that the other small velocity anomalies are not in the synthetic model (e.g., 5 and 6 in Plate 3d), the inversion with a combined anisotropic and isotropic velocity model produces an acceptable fit to the observed P-wave slab image.

5. DISCUSSION

5.1 The Cheyenne Slab

Temperature variation in the upper mantle has been suggested as the main factor affecting seismic velocities [e.g., Sobolev *et al.*, 1996; Goes and van der Lee, 2002]. However, it is unreasonable that the high velocity of the Cheyenne slab is thermally controlled if the slab is related to the Cheyenne suture formation at 1.78 – 1.75 Ga. Thermal diffusion should have erased any temperature variation within the Cheyenne slab long ago. It is also improbable for the Cheyenne slab to be a young thermal anomaly, e.g., a subducting slab or an on-going delaminating/convectively downwelling lithosphere. The Cheyenne slab is more than 1000 km inboard of the North America and Pacific plate boundary where subduction is on going. The 45° dip and the 80 km width of the Cheyenne slab is inconsistent with the predictions of most delamination models and the delamination anomalies proposed in other studies [Houseman and Molnar, 1997; Schott and Schmelling, 1998].

Our synthetic tomographic modeling (Plate 3) demonstrates a possible combined chemical and anisotropic origin for the Cheyenne slab velocity anomaly. Seismic properties of this model are consistent with the isotropically high velocity eclogitic oceanic crust and velocity anisotropy resulting from the sub-crustal olivine lattice preferred orientation (LPO) generally observed in sub-crustal oceanic lithosphere [Babuska and Cara, 1991]. Problematic is that the oceanic eclogitic crust is too thin (~8 km) to match an 80 km wide isotropic high velocity anomaly image. Thus, we propose that the Cheyenne slab's sub-crustal lithosphere is also isotropically fast with respect to the surrounding mantle.

An isotropically fast Cheyenne slab may result from the Cheyenne slab being less hydrated compared to its surroundings. This is possibly due to water removal via melting during the formation of the slab's oceanic lithosphere [Hirth and Kohlstedt, 1996]. North of the Cheyenne belt, shear wave images show that the cratonic Wyoming lithosphere is low in shear wave velocity [Goes and van der Lee, 2002; Frederiksen et al., 2001]. This observation is contrary to conventional wisdom that expects high velocity mantle beneath most Archean lithosphere [van der Lee and Nolet, 1997; Grand, 1994; James and Fouch, 2002; Freybourger et al., 2001]. The low shear wave velocities seems anomalous given the low reduced heat flow of $\sim 27 \text{ mWm}^{-2}$ [Decker et al., 1988] of the non-volcanic portions of the Wyoming Province. The Archean lower crust xenoliths found in the Leucite Hills volcanic field contain an abundance of hydrous minerals (amphibole, biotite) [Farmer et al., this volume]. If hydration occurred via a volatile flux from the mantle, it would be reasonable to assume that the Wyoming mantle lithosphere is also hydrated. South of the Cheyenne belt, post-Miocene volcanism is occurring around Steamboat Springs, Colorado, where upper mantle P- and S-velocities are low in an absolute sense [Deep Probe working group, 1998; Goes and van der Lee, 2002]. Lamproite lavas found around Steamboat Springs and Middle Park, Colorado [Thompson et al., 1997] indicate a thick (150–200 km) and hydrated lithosphere south of the Cheyenne belt. Overall, it appears plausible that a dry Cheyenne slab is isotropically fast with respect to the wetter surrounding lithospheric mantle.

Our interpretation of the high velocity anomaly as the fossil image of the north dipping Cheyenne slab is also supported by sub-crustal Eocene eruption aged eclogites and metabasites found near Cedar Mountain, Wyoming [Kuehner and Irving, 1999]. Cedar Mountain is located ~ 250 km to the west of where our seismic line crosses the Cheyenne belt (Figure 1). The geotherms calculated from the mineral assemblages suggest these rocks were erupted from 50–80 km depths. While it is difficult to constrain the emplacement history of these ultra-mafic xenoliths (i.e., fossil oceanic slab versus magmatic eclogite), this xenolith assemblage is consistent with emplacement of metamorphosed oceanic crust [Kuehner and Irving, 1999].

Shear wave splitting and receiver function studies from the CD-ROM experiment [Fox and Sheehan, this volume; Zurek and Dueker, this volume] provide more support for the north dipping Cheyenne slab anomaly. The splitting fast axis change from approximately parallel to the absolute North American plate motion direction beneath the south line to back-azimuthal-dependent north of the Cheyenne belt [Fox and Sheehan, this volume]. The forward modeling favors either a two-layer anisotropic domain or a dipping fast axis north of the Cheyenne belt. The latter is consistent with our anisotropic modeling. Receiver function analysis for the CD-ROM north line [Zurek and Dueker, this volume] shows lithospheric layering to ~ 200 km in the Archean upper mantle. Interestingly, this layering is truncated near the top of the Cheyenne slab [Plate 5 in Zurek and Dueker, this volume], and the layering is non-existent within the slab region. The slab is steeply dipping and therefore cannot be imaged with our receiver function imaging technique, but this truncation of mantle layering would be consistent with emplacement of a slab against the Wyoming cratonic margin.

5.2 Tectonic Model for Emplacement of Cheyenne Slab

Between the 2.1 Ga age of passive rift margin formation and the 1.78 Ga accretion of the Green Mountain arc, subduction polarity was south directed (i.e., outboard of the Wyoming craton) as evidenced by the lack of 2.1–1.78 Ga arc magmatic rocks north of the Cheyenne belt [Karlstrom and Houston, 1984]. If this scenario is true, then the emplacement of our north dipping Cheyenne slab demands a flip in subduction polarity post 1.78 Ga [Dueker et al., 2001; Tyson et al., 2002].

A previous tectonic model to explain the origin of the Cheyenne slab [Tyson et al., 2002; CD-ROM Working Group, 2002] suggests that the Cheyenne slab resulted from underthrusting of a ~ 200 km wide segment of the 2.1 Ga passive margin oceanic crust immediately offshore of the Wyoming passive margin. The south-directed subduction that formed the Green Mountain arc stopped at 1.78 Ga when the arc accreted to the Wyoming margin. Then, the remaining 2.1 Ga lithosphere was underthrust northward to emplace the Cheyenne slab. A concern with the Tyson model is why the 200 km oceanic lithosphere immediately south of the Wyoming passive margin would subduct beneath the Wyoming craton while the Green Mountain arc was still 200 km offshore. In the reference frame of the Wyoming craton, the force driving the closing of the ocean basin between the Green Mountain arc and the Wyoming

craton is most likely the rollback of the subducting slab. If true, it is unclear how this rollback force would instigate the subduction of the last 200 km of passive margin oceanic lithosphere.

An alternate tectonic model is that the Cheyenne slab is subducted back-arc basin lithosphere, which formed in between the Green Mountain arc and the 1.74 Ga Rawah arc accretionary event (Figure 4). Our model begins with the Green Mountain and the Rawah arcs accreted to the Wyoming craton via south dipping subduction around 1.78 Ga and 1.74 Ga, respectively (Figure 4a). After the two accretion events, a back-arc basin opened between the two arcs, due to northward-directed subduction (Figure 4b and 4c). This back-arc basin subsequently “collapsed” via a short episode of north-directed subduction beneath the Wyoming margin (Figure 4d). The small amount of subduction (~150 km) could result in no arc magmatism beneath the Green Mountain arc. Subduction flip and lack of related magmatism are commonly seen at other cratonic margins [Snyder *et al.*, 1996; Teng *et al.*, 2000; Snyder, 2002]. The ongoing collision at the North Banda Sea of the Banda arc to Australia is a modern-day example of an arc-continent collision in the process of flipping subduction polarity [Snyder *et al.*, 1996].

5.3 The Jemez Body

Given the lack of significant crustal dilatation along the Jemez suture zone, a model whereby the asthenosphere is passively pulled-up via lithospheric extension can be ruled out. Geodynamic models to explain the origin of the low velocity Jemez body thus can be separated into end-member asthenospheric and lithospheric controlled models [Dueker *et al.*, 2001]. While reviewing each model, our conclusion is that end-member models alone are not fully consistent with the seismic petrologic and geochemical observations in the study area. An interaction between the lithosphere and asthenosphere seems mostly required to explain the Jemez velocity anomaly.

An asthenospheric controlled model suggests the Jemez velocity anomaly resulting from active upwelling from upper mantle convective rolls, and/or the impact and spreading of upwelling thermals (plume). In the regional P-wave tomographic images of the western U.S [Dueker *et al.*, 2001], one of three northeast oriented low velocity trends spatially co-exists with the Jemez lineament. The alignment of these low velocity bodies with the current plate motion, and the 400-500 km spacing of these anomalies indicate that they may manifest the upwelling limbs of upper mantle convective rolls [Richter, 1973; Schmelling, 1985; Dueker *et al.*, 2001]. Upwelling thermals, as indicated by the south dipping low velocity pipe in our S-wave image, can diapirically invade and eventually move aside the lithosphere. In the convecting asthenospheric flows, it is difficult to remain any pre-existing sharp mantle layering due to the presence of chemical layers [Griffin *et al.*, 1999], juxtaposed flat slabs [Bostock, 1998], or mantle shear zones [Levin and Park, 2000]. Nevertheless, Zurek and Dueker [this volume] observed strong seismic layering co-residing with the Jemez low velocity body beneath the south line. The coexistence of the Jemez velocity anomaly with the sharp seismic layering thus strongly suggests that the Jemez anomaly is unlikely to be upwelling asthenosphere.

A lithospheric-controlled model requires that the Jemez suture contains lower-solidus materials (fertile and/or hydrated rocks in a fossil subduction zone) with respect to its surrounding mantle, and these low-solidus rocks preferentially melt during a regional heating event [Dueker *et al.*, 2001]. Low solidus mantle rocks have been reported from late Cenozoic aged mantle-derived magmas at the Navajo Volcanic Field in the Four-Corner region [Carlson and Nowell, 2001] that straddles a proposed suture zone and the northern boundary of the Proterozoic Mazatzal province [Condie, 1992]. It is possible that the hydrated materials were preserved in the Jemez suture from its formation. The most favorable evidence for the Jemez velocity anomaly being lithospheric comes from the lithospheric mantle layering [Zurek and Dueker, this volume] and the sharp lateral velocity gradient in our tomographic images. A disadvantage of the lithospheric controlled model is that the low solidus rocks needs heat input to melt at this moment in time. If early heat events initiated the melting process within the Jemez suture, the low-solidus rocks would be “depleted” long ago via melt removal.

Given that Jemez volcanism is young (the Ocate Volcanic Field above our low velocity anomaly is ~6-8 Ma old [Wood and Kienle, 1992]), it would be more reasonable to suggest that the Jemez low velocity anomaly originates from a coupled system in which the low solidus lithosphere preferentially melts in response to rising thermal currents (i.e., the low velocity pipe in our S-wave image) beneath southern Colorado and New Mexico in late Cenozoic time [Dueker *et al.*, 2001]. The impact of upwelling asthenosphere agrees with the low surface wave velocity (4.1–4.3 km/s) imaged at 100-150 km depth in this region [Goes and van der Lee, 2002; West *et al.*, 2002; Godey *et al.*, 2003]. In addition, late Cenozoic uplift [Eaton, 1982; Heller *et al.*, 2003] is also consistent with emplacement of warm buoyant mantle beneath the lithosphere.

When ascending thermals impinge upon the lithosphere, flow-induced olivine LPO aligns olivine’s fast velocity axis. As a result, the shear wave splits are expected to be in complicated patterns [Rümpker and Silver, 2000; Savage and Sheehan, 2000; Park and Levin, 2002]. Non-uniform splitting parameters have been reported in regions thought

to be undergoing small-scale convection [e.g., Gao *et al.*, 2003]. However, beneath the CD-ROM south line [Fox and Sheehan, this volume] and the RISTRA transects [Gok *et al.*, 2003], no sharp variations in the splitting parameters are observed. Given the generally poor back-azimuth sampling of the shear wave splitting results, it seems that the constraints provided from shear wave studies on lithospheric and asthenospheric fabric beneath the CD-ROM south line are rather non-unique.

A concern with our model is the heat conduction would be too slow [Turcotte and Schubert, 1982] to form the 60 km thick Jemez mantle anomaly. Advective heat transfer must have enhanced the heat transport from the asthenosphere into the lithosphere. A similar heat transport problem occurs beneath Hawaii where a broad lithospheric low P-wave velocity region (up to 5%) is observed in the oceanic lithosphere between 40 and 80 km depth [Tilman *et al.*, 2001]. Calculation shows that conductive heating by one primary conduit cannot explain the broad elongated low velocity zone. Complicated melt “pathways” are thus suggested to advect heat into a much wider region to create the broad velocity anomaly [Tilman *et al.*, 2001]. This scenario may also apply to the Jemez suture lithosphere. Asthenospheric melts are transferred into the lithosphere via extensive dyking, which significantly enhances the advective heat transport into the lithosphere, and enhances melting of low solidus minerals trapped in the Jemez suture zone.

Another puzzle with the shear wave splitting observation is the lack of variation (both azimuthal and split time) in the splitting parameters across the partially molten Jemez body. Studies of the re-heated and slightly molten peridotite samples from the Ronda massif (Spain) show that the olivine LPO remains unperturbed even after the heating and partial melting event [Vauchez and Carlos, 2001]. The Jemez body may represent a region where small amount of the melts (i.e., 0.5 %) is present, which would cause large velocity reductions [Hammond and Humphreys, 2000], yet still retain an undisturbed olivine LPO.

6. CONCLUSION

The CD-ROM passive seismic results suggest that fossil lithospheric heterogeneities have been preserved beneath the two primary suture zones in the southern Rocky Mountains Lithosphere (Plate 4). A high velocity Proterozoic slab fragment exists beneath the Cheyenne belt. The slab is high velocity probably due to some combination of eclogitic facies oceanic crust, frozen-in oceanic olivine LPO, and/or the juxtaposition of this fossil slab against hydrated mantle. A low velocity Jemez body resides beneath the Jemez suture. The low velocity anomaly most probably represents low solidus materials preserved in the Jemez suture lithosphere, and is now molten due to a late Cenozoic regional heating event. These observations suggest that a thick chemical lithosphere is present in the Rock Mountain regions, down to 200 km beneath the Cheyenne belt, and 100 km under the Jemez suture.

Acknowledgments. We thank Matthew Fouch, Aibing Li and Michael West for valuable comments and help for improving the manuscript. We also thank the CD-ROM group led by Karl Karlstrom, the IRIS PASSCAL Instrument Center, and the NSF Continental Dynamics Program. The work was funded by NSF Continental Dynamics grant 0614410.

REFERENCE

- Abramovitz, T., and H. Thybo, Seismic images of Caledonian, lithosphere-scale collision structures in the southeaster North Sea along MONA LISA Profile 2, *Tectonophysics*, 317, 27-54, 2000.
- Aldrich, M.J., and A.W. Laughlin, A model for the tectonic development of the southeastern Colorado Plateau boundary, *J. Geophys. Res.*, 89, 10207-10218, 1984.
- Allen, R.M., G. Nolet, W.J. Morgan, K. Vogfiord, B.H. Bergsson, P. Erlendsson, G.R. Foulger, S. Jakobsdottir, B.R. Julian, M. Pritchard, S. Ragnarsson, and R. Stefansson, Imaging the mantle beneath Iceland using integrated seismological techniques, *J. Geophys. Res.*, 107, 2001JB000595, 2002.
- Armstrong, R.L., and P. Ward, Evolving geographic patterns of Cenozoic magmatism in the North American cordillera: the temporal and spatial association of magmatism and metamorphic core complexes, *J. Geophys. Res.*, 34, 149-164, 1991.
- Babuska, V., and M. Cara, *Seismic anisotropy in the Earth*, Kluwer Academic, Dordrecht, 1991.
- Baldrige, W.S., G.R. Keller, V. Haak, E. Wendlandt, G.R. Jiracek, and K.H. Olsen, *The Rio Grande Rift*, Elsevier, 1995.
- Balling, N., Deep seismic reflection evidence for ancient subduction and collision zones within the continental lithosphere of northwestern Europe, *Tectonophysics*, 329, 269-300, 2000.
- Bostock, M.G., Mantle stratigraphy and evolution of the Slave province, *J. Geophys. Res.*, 103, 21183-21200, 1998.
- Carlson, R.W., and G.M. Nowell, Olivine-poor sources for mantle-derived magmas: O_s and H_f isotopic evidence from potassic magmas of the Colorado Plateau, *Geochem. Geophys. Geosyst.*, 2, 2000GC000128, 2001.
- CD-ROM Working Group, Structure and evolution of the lithosphere beneath the Rocky Mountains: initial results from the CD-ROM experiment, *GSA Today*, 10, 4-10, 2002.

- Chamberlain, K.R., Medicine Bow orogeny: Timing of deformation and model of crustal structure produced during continent-arc collision, ca 1.78 Ga, southeastern Wyoming, *Rocky Mountain Geology*, 33, 259-277, 1998.
- Chapin, C.E., Evolution of the Rio Grande rift - A summary, in *Rio Grande Rift: Tectonics and Magmatism*, edited by R.E. Riecker, American Geophysical Union, Washington D.C., 1979.
- Condie, K.C., Proterozoic terranes and continental accretion in southwestern North America, in *Proterozoic crustal evolution*, edited by K.C. Condie, pp. 447-480, Elsevier, 1992.
- Decker, E.R., H.P. Heasler, K.L. Buelow, K.H. Baker, and J.S. Hallin, Significance of past and recent heat flow and radioactivity studies in the southern Rocky Mountains region, *Geological Society of America Bulletin*, 100, 1851-1885, 1988.
- Deep Probe working group, Probing the Archean and Proterozoic lithosphere of western North America, *GSA Today*, 8, 1-7, 1998.
- Dueker, K., E.D. Humphreys, and G. Biasi, Teleseismic imaging of the western United States upper mantle structure using the simultaneous iterative reconstruction technique, in *Seismic Tomography*, edited by K. Hirahara, pp. 265-298, Chapman & Hall, London, 1993.
- Dueker, K., H. Yuan, and B. Zurek, Thick Proterozoic lithosphere of the Rocky Mountain region, *GSA Today*, 11, 4-9, 2001.
- Dziewonski, A.M., and D.L. Anderson, Travel-time and station corrections for P-waves at teleseismic distances, *J. Geophys. Res.*, 88, 722-743, 1983.
- Eaton, D.W., and J.F. Cassidy, A relic Proterozoic subduction zone in western Canada: New evidence from seismic reflection and receiver function data, *Geophys. Res. Lett.*, 23, 3791-3794, 1996.
- Eaton, G.P., The basin and Range province: Origin and tectonic significance, *Annual Review of earth and Planetary Sciences*, 10, 409-440, 1982.
- Farmer, L., S. Bowring, N. Christensen, M. Williams, J. Matzel, and L. Stevens, Contrasting lower crustal evolution across an Archean-Proterozoic suture: Physical, Chemical and Geochronologic studies of lower crustal xenoliths in southern Wyoming and northern Colorado, this volume.
- Fox, O., and A.F. Sheehan, Shear wave splitting beneath the CD-ROM transects, this volume.
- Frederiksen, A.W., M.G. Bostock, and J.F. Cassidy, S-wave velocity structure of the Canadian upper mantle, *Physics of the Earth and Planetary Interiors*, 124, 175-191, 2001.
- Freybourger, M.J., J.B. Gaherty, and T. Jordan, Structure of the Kaapvaal craton from surface waves, *Geophys. Res. Lett.*, 28, 2489-2492, 2001.
- Gao, S.S., K.H. Liu, P.M. Davis, P.D. Slack, Y.A. Zorin, V.V. Mordvinova, and V.M. Kozhevnikov, Evidence for small-scale mantle convection in the upper mantle beneath the Baikal rift zone, *J. Geophys. Res.*, 108, 10.1029/2002JB002039, 2003.
- Godey, S., R. Snieder, A. Villasenor, and H.M. Benz, Surface wave tomography of North America and the Caribbean using global and regional broad-band networks: Phase velocity maps and limitations of ray theory, *Geophys. J. Int.*, 152, 620-632, 2003.
- Goes, S., and S. van der Lee, Thermal structure of the North American uppermost mantle, *J. Geophys. Res.*, 107, 2000JB000049, 2002.
- Gorman, A.R., R.M. Clowes, R.M. Ellis, T.J. Henstock, G.D. Spence, G.R. Keller, A. Levander, C.M. Snelson, M.J.A. Buriannyk, E.R. Kanasevich, I. Asudeh, Z. Hajnal, and K.C. Miller, Deep Probe: Imaging the roots of western North America, *Canadian Journal of Earth Sciences*, 39, 375-398, 2002.
- Grand, S., Mantle shear structure beneath the Americas and surrounding oceans, *J. Geophys. Res.*, 99, 11591-11621, 1994.
- Grand, S., and D.V. Helmberger, Upper mantle shear structure of North America, *Geophys. J. R. astr. Soc.*, 76, 399-438, 1984.
- Griffin, W.L., S.Y. O'Reilly, R. Davies, K. Kivi, E. van Achterbergh, L.M. Natapov, B.J. Doyle, C.G. Ryan, and N.J. Pearson, Layered mantle lithosphere in the Lac de Gras area, Slave craton: Composition, structure and origin, *Journal of Petrology*, 40, 705-727, 1999.
- Hamilton, W., and W.B. Myers, Cenozoic tectonics of the western United States, *Reviews of Geophysics*, 4, 509-549, 1966.
- Hammond, W.C., and E.D. Humphreys, Upper mantle seismic wave velocity: effects of realistic partial melt geometries, *J. Geophys. Res.*, 105, 10975-10986, 2000.
- Heller, P.L., K. Dueker, and M.E. McMillan, Post-Paleozoic alluvial gravel transport as evidence of continental tilting in the U.S. Cordillera, *Geological Society of America Bulletin*, 115, 1122-1132, 2003.
- Hirth, G., and D.L. Kohlstedt, Water in the oceanic upper mantle: Implications for rheology, melt extraction and the evolution of lithosphere, *Earth Planet. Sci. Lett.*, 144, 93-108, 1996.
- Houseman, G.A., and P. Molnar, Gravitational (Rayleigh-Taylor) instability of a layer with non-linear viscosity and convective thinning of continental lithosphere, *Geophysical Journal International*, 128, 125-150, 1997.
- Ingersoll, R.V., W. Cavazza, W.S. Baldrige, and M. Shafiqullah, Cenozoic sedimentation and paleotectonics of north-central New Mexico: Implications for initiation and evolution of the Rio Grande rift, *Geological Society of America Bulletin*, 102, 1280-1296, 1990.
- James, D.E., and M.J. Fouch, Formation and evolution of Archean cratons: insights from southern Africa, in *The Early Earth: Physical, Chemical and biological Development*, edited by C.J. Hawkesworth, pp. 1-26, Spec. Pub., London, 2002.
- Judenherc, S., M. Granet, J.P. Brun, G. Poupinet, J. Plomerova, A. Mocquet, and U. Achauer, Images of lithospheric heterogeneities in the armorican segment of the Hercynian Range in France, *Tectonophysics*, 358, 121-134, 2002.
- Karato, S., Importance of anelasticity in the interpretation of seismic tomography, *Geophys. Res. Lett.*, 20, 1623-1626, 1993.
- Karato, S., and H. Jung, Water, partial melting and the origin of the seismic low velocity and high attenuation zone in the upper mantle, *Earth Planet. Sci. Lett.*, 157, 193-207, 1998.

- Karlstrom, K.E., and S.A. Bowring, Early Proterozoic assembly of tectonostratigraphic terranes in southwestern North America, *Journal of Geology*, 96, 561-576, 1988.
- Karlstrom, K.E., and R.S. Houston, The Cheyenne belt: analysis of a Proterozoic suture in southern Wyoming, *Precambrian research*, 25, 415-446, 1984.
- Karlstrom, K.E., and E.D. Humphreys, Persistent influence of Proterozoic accretionary boundaries in the tectonic evolution of southwestern North America: Interaction of cratonic grain and mantle modification events, *Rocky Mountain Geology*, 33, 161-179, 1998.
- Kennett, B.L.N., and E.R. Engdahl, Traveltimes for global earthquake location and phase identification, *Geophys. J. Int.*, 105, 429-465, 1991.
- Kluth, C.F., and P.J. Coney, Plate tectonics of the Ancestral Rocky Mountains, *Geology*, 9, 10-15, 1981.
- Kuehner, S.M., and A.J. Irving, Eclogite and metabasite xenoliths of subducted slab origin from the Paleogene Cedar Mountain diatremes, southwestern Wyoming, USA, *Proceedings of the International Kimberlite Conference*, 1, 485-493, 1999.
- Levin, V., and J. Park, Shear zones in the Proterozoic lithosphere of the Arabian shield and the nature of the Hales discontinuity, *Tectonophysics*, 323, 131-148, 2000.
- Magnani, M.B. and A. Levander, Listric thrust faulting in the Laramide front of north-central New Mexico guided by Precambrian basement anisotropies, this volume.
- Meyerholtz, K.A., G.L. Pavlis, and S.A. Szpakowski, Convolutional quelling in seismic tomography, *Geophysics*, 54, 570-580, 1989.
- Morgan, R.P.L., P.J. Barton, M. Warner, J. Morgan, C. Price, and K. Jones, Lithospheric structure north of Scotland-I.P-wave modeling, deep reflection profiles and gravity, *Geophys. J. Int.*, 142, 716-736, 2000.
- Park, J., and V. Levin, Seismic anisotropy: Tracing plate dynamics in the mantle, *Science*, 296, 485-489, 2002.
- Pharaoh, T.C., Paleozoic terranes and their lithospheric boundaries within the Trans-European suture zone (TESZ): a Review, *Tectonophysics*, 314, 17-41, 1999.
- Poupinet, G., N. Arndt, and P. Vacher, Seismic tomography beneath stable tectonic regions and the origin and composition of the continental lithospheric mantle, *Earth Planet. Sci. Lett.*, 212, 89-101, 2003.
- Rümpker, G., and P. G. Silver, Calculating splitting parameters for plume-type anisotropic structures of the upper mantle, *Geophys. J. Int.* 143, 507-520, 2000
- Richter, F.M., Dynamical models for sea floor spreading, *Reviews of Geophysics and Space Physics*, 11, 223-287, 1973.
- Sandoval, S., E. Kissling, J. Ansorge, and the SVEKALAPKO Seismic Tomography Working Group, High-resolution body wave tomography beneath the SVEKALAPLO array: II. Anomalous upper mantle structure beneath the central Baltic Shield, *Geophys. J. Int.*, submitted, 2003a.
- Sandoval, S., E. Kissling, J. Ansorge, and "the SVEKALAPKO Seismic Tomography Working Group", High-resolution body wave tomography beneath the SVEKALAPLO array: I. A priori three-dimensional crustal model and associated traveltime effects on teleseismic wave fronts, *Geophys. J. Int.*, 153, 75-87, 2003b.
- Saruwatari, K., S. Ji, C. Long, and M. Salisbury, Seismic anisotropy of mantle xenoliths and constraints on upper mantle structure beneath the southern Canadian Cordillera, *Tectonophysics*, 339, 403-426, 2001.
- Savage, M.K., and A.F. Sheehan, Seismic anisotropy and mantle flow from the Great Basin to the Great Plains, western United States, *J. Geophys. Res.*, 105, 13715-13734, 2000.
- Schmelling, H., Numerical models on the influence of partial melt on elastic, anelastic and electric properties of rocks, Part I: elasticity and anelasticity, *Physics of the Earth and Planetary Interiors*, 41, 34-57, 1985.
- Schott, B., and H. Schmelling, Delamination and detachment of a lithospheric root, *Tectonophysics*, 296, 225-247, 1998.
- Schutt, D.L., and E.D. Humphreys, P and S wave velocity and Vp/Vs in the wake of the Yellowstone Hotspot, *J. Geophys. Res.*, in press.
- Shaw, C.A., and K.E. Karlstrom, The Yavapai-Mazatzal crustal boundary in the southern Rocky Mountains, *Rocky Mountain Geology*, 34, 37-52, 1999.
- Shearer, P.M., *Introduction to Seismology*, Cambridge University Press, New York, 1999.
- Shomali, Z.H., R.G. Roberts, and the TOR Working Group, Non-linear body wave teleseismic tomography along the TOR array, *Geophys. J. Int.*, 148, 562-574, 2002.
- Shragge, J., M.G. Bostock, C.G. Bank, and R.M. Ellis, Integrated teleseismic studies of the southern Alberta upper mantle, *Canadian Journal of Earth Sciences*, 39, 399-411, 2002.
- Snelson, C.M., H.M. Rumpel, G.R. Keller, K.C. Miller, and C. Prodehl, Regional crustal structure derived from the CD-ROM seismic refraction/wide-angle reflection experiment: The lower crustal and upper mantle, this volume.
- Snyder, D.B., Lithospheric growth at margins of cratons, *Tectonophysics*, 355, 7-22, 2002.
- Snyder, D.B., H. Prasetyo, Blundell, D. J., C.J. Pigram, A.J. Barber, A. Richardson, and S. Tjokosaprotro, A dual doubly-vergent orogen in the Banda Arc continent-arc collision zone as observed on deep seismic reflection profiles, *Tectonics*, 15, 34-53, 1996.
- Sobolev, S.V., A. Gresillaud, and M. Cara, How robust is isotropic delay time tomography for anisotropic mantle?, *Geophys. Res. Lett.*, 24, 509-512, 1999.
- Soedjatmiko, B., and N.I. Christensen, Seismic anisotropy under extended crust: evidence from upper mantle xenoliths, Cima volcanic field, California, *Tectonophysics*, 321, 279-296, 2000.
- Teng, L., S., C.T. Lee, Y.B. Tsai, and L.Y. Hsiao, Slab breakoff as a mechanism for flipping of subduction polarity in Taiwan, *Geology*, 28, 155-158, 2000.

- Thompson, R.N., J.G. Mitchell, A.P. Dickin, S.A. Gibson, D. Velde, P.T. Leat, and M.A. Morrison, Oligocene lamproites containing an Al-poor, Ti-rich biotite, Middle Park, northwest Colorado, USA, *Mineralogical Magazine*, *61*, 557-572, 1997.
- Tilmann, F.J., H.M. Benz, K.F. Priestley, and P.G. Okubo, P wave velocity structure of the uppermost mantle beneath Hawaii from travel time tomography, *Geophys. J. Int.*, *146*, 594-606, 2001.
- Turcotte, D., and G. Schubert, *Geodynamics: Applications of continuum physics to geological problems*, 450 pp., John Wiley and Sons, New York, 1982.
- Tyson, E., K.E. Morozova, K.E. Karlstrom, K.R. Chamberlain, S.B. Smithson, K.G. Dueker, and C.T. Foster, Proterozoic Farewell Mountain-Lester Mountain suture zone, northern Colorado: Subduction flip and progressive assembly of arcs, *Geology*, *30*, 943-946, 2002.
- van der Lee, S., and G. Nolet, Upper mantle S velocity structure of North America, *J. Geophys. Res.*, *102*, 22815-22838, 1997.
- VanDecar, J.C., and R.S. Crosson, Determination of teleseismic relative phase arrival times using multi-channel cross correlation and least squares, *Bull. Seismol. Soc. Am.*, *80*, 150-159, 1990.
- Vauchez, A., and J.G. Carlos, Seismic properties of an asthenospherized lithospheric mantle: constraints from lattice preferred orientations in peridotite from the Ronda Massif, *Earth Planet. Sci. Lett.*, *192*, 235-249, 2001.
- Warner, M., J. Morgan, P. Barton, C. Price, and K. Jones, Seismic reflections from the mantle represent relict subduction zones within the continental lithosphere, *Geology*, *24*, 39-42, 1996.
- Warren, L.M., and P.M. Shearer, Investigating the frequency dependence of mantle Q by stacking P and PP spectra, *J. Geophys. Res.*, *105*, 25391-25402, 2000.
- West, M., J. Ni, D. Wilson, R. Aster, S. Grand, W. Gao, R. Gok, S. Baldrige, S. Semken, and J. Schlue, Structure of the uppermost mantle beneath the RISTRA array from surface waves, *AGU 2002 Fall Meet. Suppl., Abstract S61A-1116*, 2002.
- White, D.J., S.B. Luca, W. Bleeker, Z. Hajnal, J.F. Lewry, and H.V. Zwanig, Suture-zone geometry along an irregular Paleoproterozoic margin: The Superior boundary zone, Manitoba, Canada, *Geology*, *30*, 735-738, 2002.
- Williams, M.L., K.E. Karlstrom, A. Lanzirotti, A.S. Read, J.L. Bishop, C.E. Lombardi, J.N. Pedrick, and M.B. Wingsted, New Mexico middle crustal cross sections: 1.65 Ga macroscopic geometry, 1.4 Ga thermal structure and continued problems in understanding crustal evolution, *Rocky Mountain Geology*, *34*, 53-66, 1999.
- Wood, C.A., and J. Kienle, *Volcanoes of North America: United States and Canada*, 354 pp., Cambridge University Press, 1992.
- Wooden, J.L., and E. DeWitt, Pb isotopic evidence for a major early crustal boundary in western Arizona, in *Proterozoic geology and ore deposits of Arizona*, edited by K.E. Karlstrom, Arizona Geological Society Digest, 1991.
- Zurek, B., and K. Dueker, Images of lithospheric stratigraphy beneath the CD-ROM lines, this volume.

FIGURE CAPTIONS

Figure 1. Crustal provinces of the southern Rockies and CD-ROM transects (black triangles). Geographic labels are: GF, Geochron Front [Chamberlain, 1998]; CB, Cheyenne belt; FM-LM, Farewell Mountain-Lester Mountain shear zone that separates the Green mountain and Rawah arcs; SL, San Luis basin; JT, the Jemez volcanic trend/suture; GP, the Great Plains; CM, Cedar Mountains; LH, Leucite Hills; NVF, Navajo Volcanic Field; and MP, Middle Park. Tomographic images are presented along A-A'.

Figure 2. Station median residuals for two back-azimuth quadrants, the southeast (open circles) and the northwest (crosses). (a) P-wave residuals. (b) S-waves residual. Note the large peak-to-peak residual amplitudes (1.4 and 3.7 sec for P and S, respectively), and strong azimuthal variations across the Cheyenne belt (CB) and the Jemez volcanic trend/suture (JT).

Figure 3. S-wave velocity variations of the Cheyenne slab for the two different S-wave dataset. a) For the maximum particle motion direction. b) For the average fast velocity direction. Note the Cheyenne slab breaks at 2.6% velocity variation level in a).

Figure 4. Cartoon of subduction polarity flip to emplace the Cheyenne slab. (a) Pre- 1.78 Ga while the Green Mountain Arc (GMA) and the Rawah Arc (RA) were being formed offshore via south dipping subduction. Arrows show the subduction direction. The Cheyenne belt (CB) formed at ~1.78 Ga after the Green Mountain Arc accreted to the Wyoming passive margin. The accretion of the Rawah arc occurred at 1.74 Ga [Tyson et al., 2002]. (b) After the Rawah Arc accreted to the Green Mountain Arc, a back-arc basin is opened, due to later north-directed subduction. (c) The opening of the back-arc basin formed a ~200 km wide section of oceanic lithosphere. (d) The closure of the basin resulted via north-directed subduction emplaced the Cheyenne slab against the Archean mantle keel.

Plate 1. Crust and mantle resolution tests. Input models are parameterized by amplitude ratio θ between the crust and mantle, and spatial wavelength λ_c (for the crust) and λ_m (for the mantle) of the synthetic velocity variations. (a) Crust model with $\theta = 3$, $\lambda_c = 30$ km and $\lambda_m = 90$ km. (b) Inverted crust model. (c) Mantle model $\theta = 1/2$, $\lambda_c = 60$ km and $\lambda_m = 90$ km. (d) Inverted mantle model.

Plate 2. Tomographic inversion results. (a) The P-wave image. (b) The S-wave image inverted using the dataset measured in the maximum particle motion coordinate system. Blue and red denote high and low velocity variations. Triangles at zero depth are stations. Variance reduction is 84% and 81% for the P and S image, respectively. Note the 3 major anomalies, the Cheyenne slab, the Jemez body and the low velocity pipe (more obvious in the S-wave image). (c) Standard errors of the velocity models. (d) Selected resolution kernels for the P-wave inversion. The Cheyenne slab, the Jemez body and the low velocity pipe are in regions with low standard error and compact resolution kernels. The standard error and resolution kernels for the S-wave image are similar to this figure, except that the standard error amplitudes range from 0.5% - 0.9%.

Plate 3. P-wave anisotropic synthetic inversions. The input model is defined as the 2% contour region of the P-wave Cheyenne slab. (a) Image for the isotropic model with 2% isotropic velocity variation within the slab. (b) Image for the anisotropic model. An 8% dipping fast velocity anisotropy is assigned to the slab. The ellipse to the upper right corner illustrates the simplified velocity tensor for the assigned anisotropy with its fast and slow axes labeled as F and S, respectively. (c) Inverted image for the combined anisotropic and isotropic model. (d) Observed P-wave image. Triangles at zero depth represent stations. Colorbar for the synthetics (a, b, and c) is scaled to 80% of the observed image (d). Visual comparisons with the observed P-wave image suggest that the image of the combined model best matches the observed image best (regions 1 - 4). Note in the input synthetic models other small anomalies (5 and 6) are not modeled.

Plate 4. Cartoon of the southern Rocky Mountains lithosphere beneath the CD-ROM transect. Labels are: HP, High Plains; SL, San Luis basin, and OVF, Ocate volcanic field. The northern extent of the lithosphere/asthenosphere boundary (LAB) is drawn based upon the following structural elements: the depth extent of Cheyenne slab velocity image; receiver function layering [Zurek and Dueker, this volume]; the Stateline kimberlite pipes [Lester and Farmer, 1998]; the Middle Park Lamproites (MPL), and the Cedar Mountain (CM) eclogites and metabasites. Variations in shear wave splitting measurements occur north of the Cheyenne belt, while the shear wave measurements are uniform to the south. Receiver functions [Zurek and Dueker, this volume] show imbricated Moho beneath the Cheyenne belt (CB). The southern position of the LAB is based upon the receiver function layering within the Jemez low velocity anomaly to 100 km. The low velocity asthenosphere [Goes and van der Lee, 2002; West et al., 2002] probably was formed after the impact of upwelling thermals, and provides heat input to the southern line lithosphere.

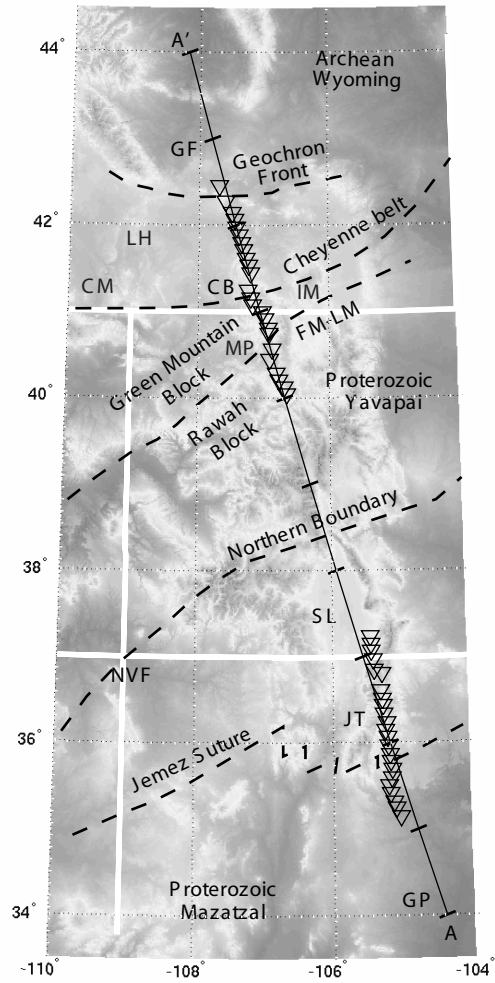


Figure 1

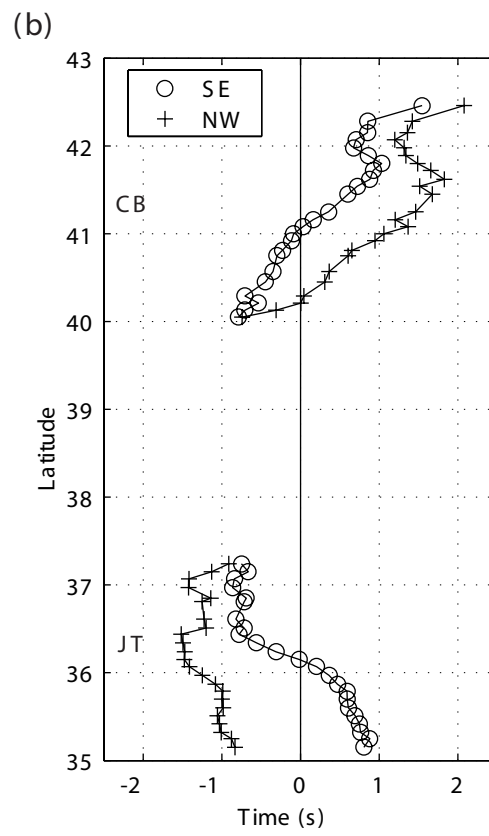
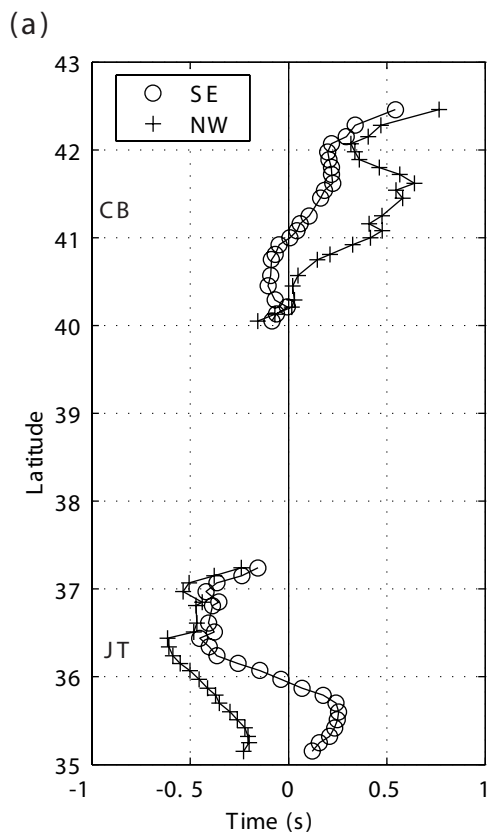


Figure 2

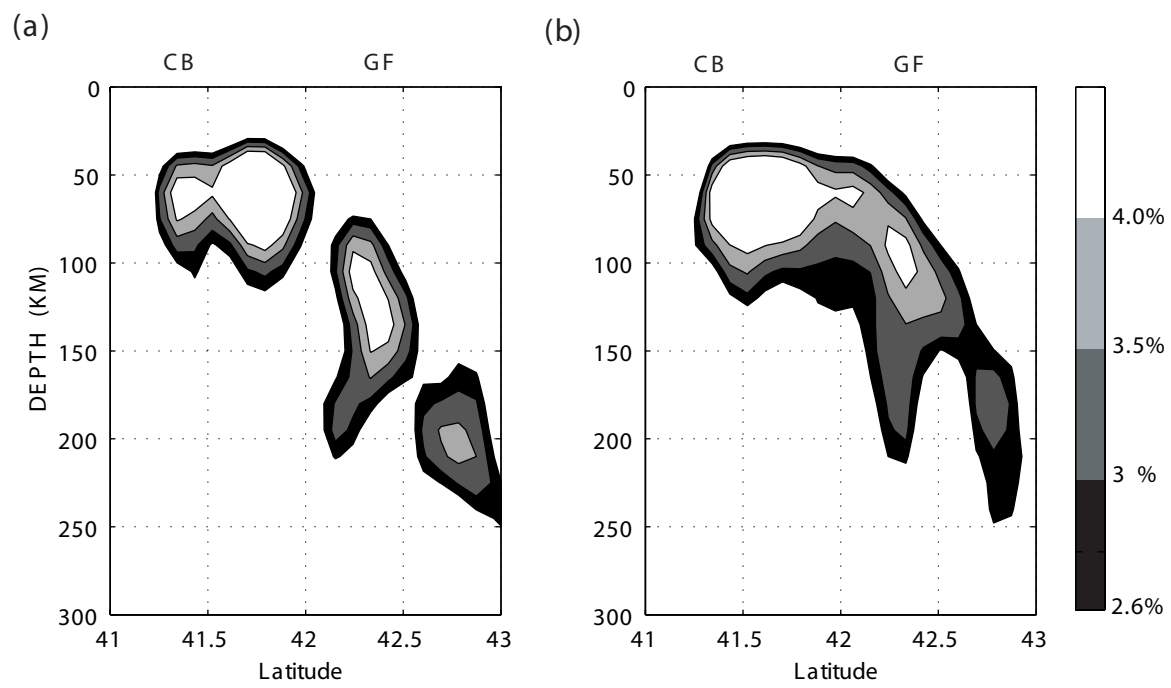


Figure 3

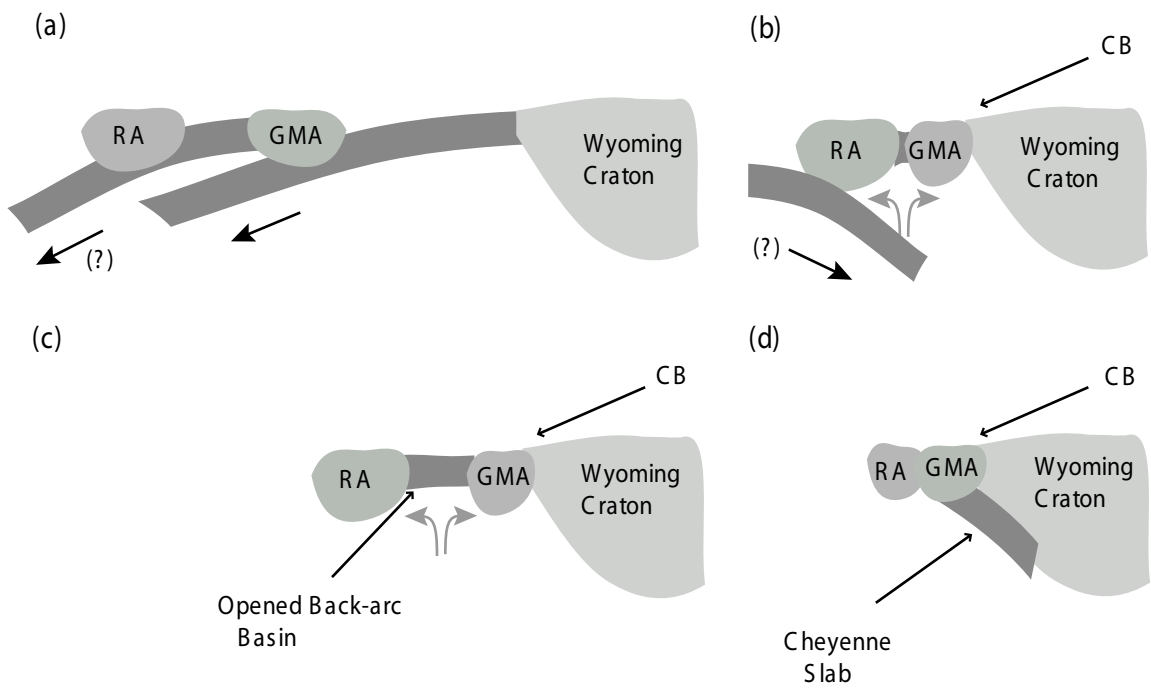


Figure 4

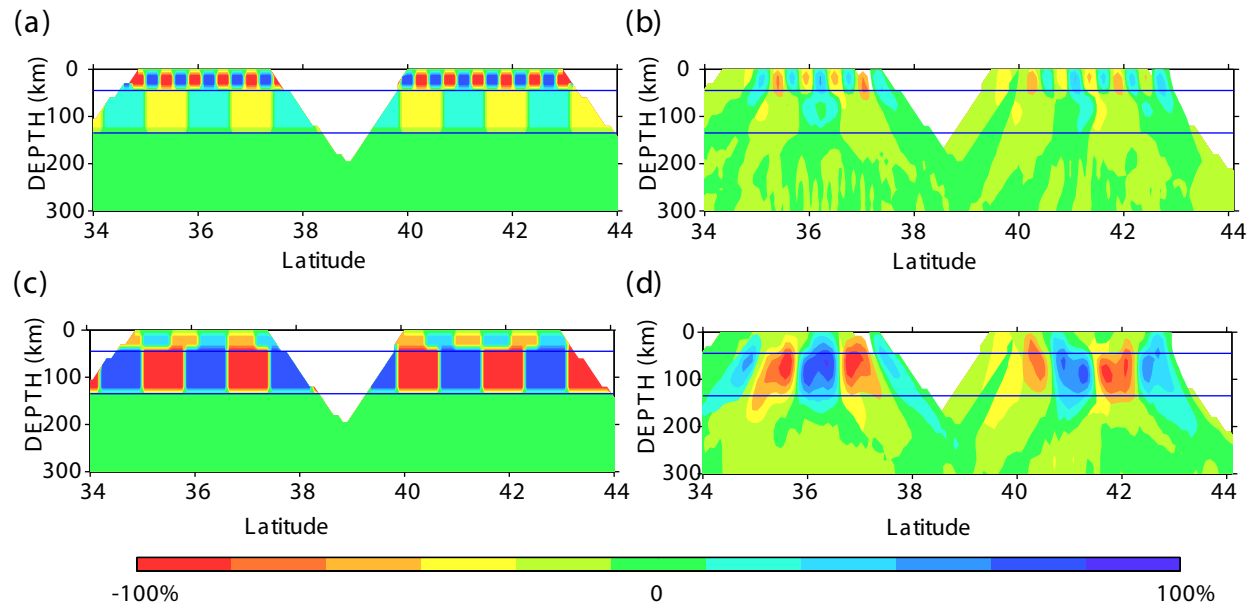


Plate1

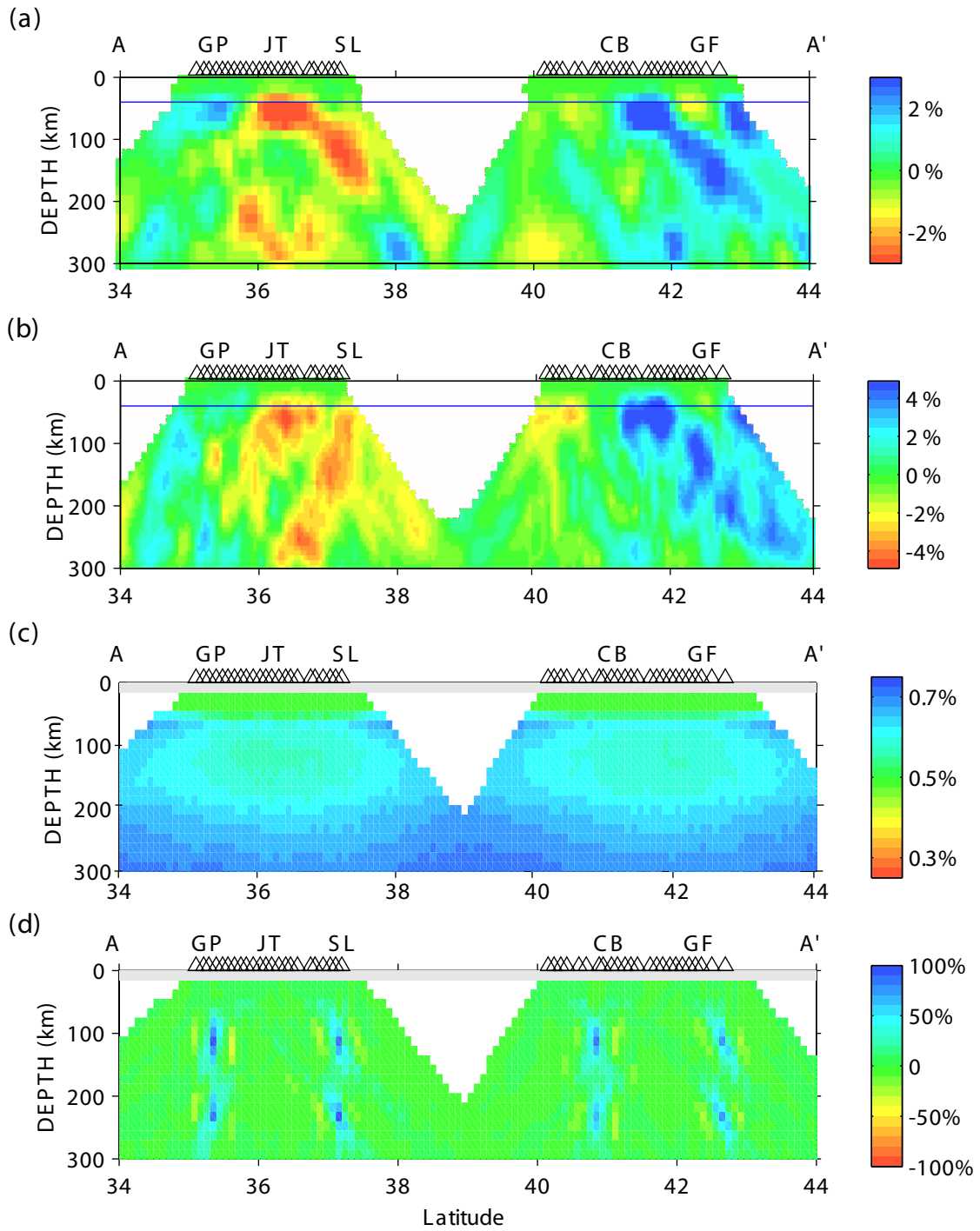


Plate 2

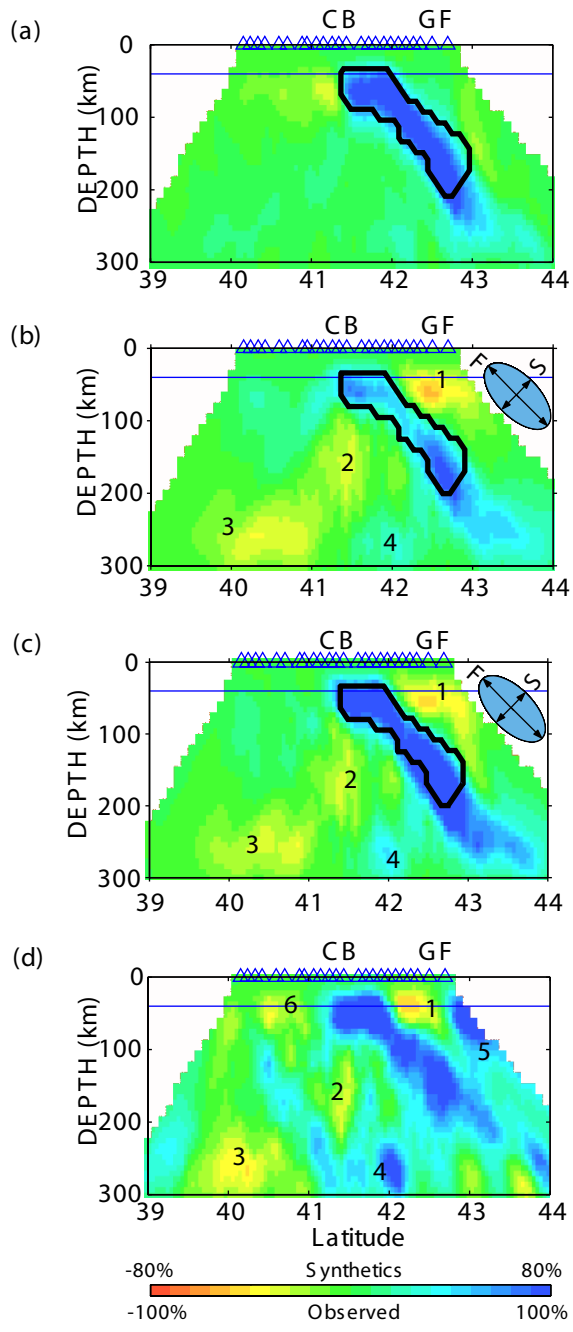


Plate 3

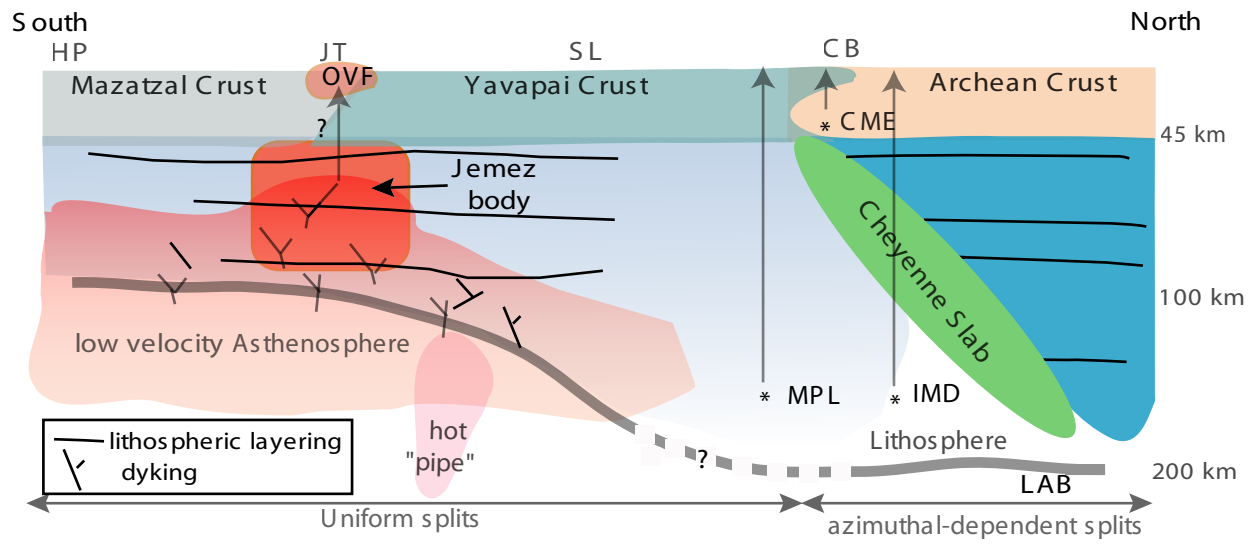


Plate 4